Scale Effects on Solid-Propellant Coaxial Magnetoplasmadynamic Thruster Performance

Giorgio Paccani[*] and Luigi Petrucci[†]
University of Rome "La Sapienza," 00184 Rome, Italy
and
William D. Deininger[‡]

Ball Aerospace and Technologies Corp., Boulder, Colorado 80306

An experimental investigation of solid-propellant, nonsteady (pulse durations of ∼1 ms), magnetoplasmadynamic (MPD) thruster operation as a function of thruster scale (size) is qualitatively discussed. Measurements include the electrical characteristics, impulse bit (thrust stand), exhaust velocity (time-of-flight Langmuir probe system), and ablated propellant mass for each scaled thruster. The same number of thruster shots is used to collect data at each operating point. The baseline thruster is found to operate in one of two electrical modes (high and low), in a random fashion, at a fixed energy. As the absolute energy level is increased, the probability of high-mode operation is found to increase. The scaled thrusters (33% smaller and 25% larger based on nozzle exit radius) operate in only one electrical mode. Furthermore, these tests show that the smaller thruster's operating characteristics at equal thruster energy exhibit higher currents, impulse bits, and propellant consumption, whereas the other two thrusters show the effective Maecker's law coefficient b_{eff} increasing as a function of the time integral of the MPD discharge squared current Ψ, as well as the thruster efficiency increasing with thruster energy. These data imply that the smaller thruster operates in a different regime than the larger thrusters. This operational regime difference is likely related to the smaller thruster's higher current densities at constant thruster energy.

Nomenclature

b	=	Maecker's law[13] coefficient, N/A^2
E	=	energy, J
I_b	=	impulse bit, N · s
i	=	current, A
m	=	ablated mass per shot, kg
Re_m	=	magnetic Reynolds number
r	=	radius, m
t	=	time, s
V	=	potential, V
w	=	exhaust velocity, m/s
Z	=	impedance, Ω
η	=	efficiency
μ_0	=	magnetic permeability of free space, 12.57 Wb · A^{-1}m^{-1}
ρ	=	anode-to-cathode radius ratio
σ	=	electrical conductivity, $\Omega^{-1} \cdot$ m^{-1}
Ψ	=	$\int i^2 \, dt$, A^{2}s
ω	=	frequency, s^{-1}

Subscripts

a	=	anode
c	=	cathode
eff	=	effective
j	=	jet
max	=	maximum
med	=	medium
min	=	minimum
sp	=	specific
T	=	thruster
th	=	theoretical

Introduction

SOLID-PROPELLANT electromagnetic thrusters are receiving increasing attention due to their simple, robust designs, relatively high specific impulse, and well-defined impulse bit delivery capability. This class of electromagnetic thruster uses solid propellants such as Teflon®, meaning that the propellant flow rate is not an externally controllable variable, but is determined by the propellant properties, engine geometry, and the arc–propellant interaction.[1] Previous work examined solid-propellant magnetoplasmadynamic (MPD) performance as a function of propellant material[2] where Teflon was validated as one of the better propellant options.

Engine scale, or size, is a geometric parameter that can affect engine performance. Some testing on gas-fed MPD thrusters of different sizes has been conducted,[3–6] with more limited testing of scaled solid-propellant MPD thrusters.[7] This paper will qualitatively describe and discuss the results of an experimental activity aimed at investigating scale effects on the behavior of nonsteady, ablative, coaxial MPD thrusters (electrical characteristics and performance).[8] The MPD thrusters are operated with instantaneous power levels of a few megawatts during pulses (shots) that last approximately 1 ms. Three scaled thrusters, a nominal baseline (MIRA) thruster, one 33% smaller (MIRA-S) and another 25% larger (MIRA-L), were fabricated and tested.

Experimental Setup

The thruster system and facilities used for the experiments discussed in this paper are summarized in this section. The test procedures and measurements are also covered.

MPD Thruster System

The MPD thruster system consists of an energy storage and transmission network, an MPD accelerator and a start-up circuit.

The energy storage and transmission network[9] consists of a pulse-forming network (PFN) made up of 30 elements connected in

Fig. 1   Thrust balance layout.

Table 1   Scaled MPD thruster key dimensions

Parameter	MIRA-S	MIRA	MIRA-L
Nozzle half-angle, deg	22.5	22.5	22.5
Cathode radius, mm	6.75	9.0	11.25
Anode throat radius, mm	17.5	23.5	29.5
Trigger electrode diameter, mm	1.5	2.0	2.5
Cathode/throat radii ratio	0.38	0.43	0.39
Area ratio	5.39	5.48	5.56

Fig. 2   Baseline MIRA solid-propellant MPD thruster.
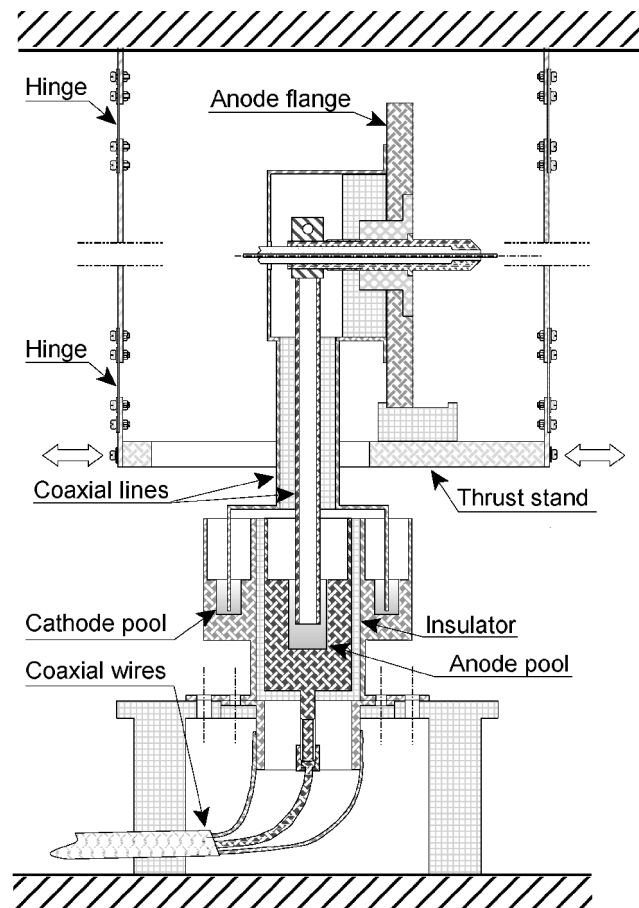
parallel. Each of these elements include an electrolytic capacitor, with a nominal peak voltage rating of 450 V, connected in parallel with an inductor of 8.4×10^{-7} H. The elements are assembled into two parallel and equal branches of 15 capacitors/inductors, each of which are tied coaxially to the MPD electrodes and provide a total measured capacitance of 0.072 ± 0.002 F. The PFN set voltage was the primary externally controllable variable during the tests.

A coaxial transmission line is used between the PFN and thrust stand inside the vacuum chamber. Because the thrust stand must oscillate freely to enable accurate thrust measurements, concentric mercury pools are used to transmit the power to the MPD accelerator, as shown in Fig. 1.

The baseline MPD thruster is shown in Fig. 2 and has been described in detail elsewhere.[8] It uses a flared or conical nozzle, which has been shown to provide improved performance compared to other geometries.[5,7,10] Briefly, the MIRA thruster consists of a conical anode nozzle with an area ratio of 5.48–1.0 that coaxially surrounds the cathode. The anode is fabricated from an aluminum–silicon–manganese alloy (anticorodal) (stainless steel is used for the smallest thruster), has a throat radius of 23.5 mm and an exit radius of 55 mm. The 18- mm-diam cathode is made from copper (lanthanated tungsten is used for the smallest thruster). The anode-to-cathode radius ratio ρ, calculated assuming the minimum, medium, and maximum anode radii, are, respectively,

$$\rho_{\min} = 2.6, \qquad \rho_{\mathrm{med}} = 4.3, \qquad \rho_{\max} = 6.1$$

The MIRA-L and MIRA-S scaled thrusters were also fabricated and tested.

Six Teflon propellant bars, with a section of 3×10 mm, pass radially through the wall of the nozzle and symmetrically surround the cathode tip.

A 2-mm-diam trigger electrode, which is located coaxially within the MPD cathode and protrudes approximately 10 mm, is used to initiate the discharge. The trigger electrode is isolated from the MPD cathode by a coaxial hollow sleeve of Teflon. The discharge is initiated through a several microsecond voltage pulse of ~10 kV, with an energy of about 1 J, using a 0–20 kV power supply connected to the tungsten trigger electrode.

The smaller thruster is fabricated from different materials than the larger thrusters due to the higher current densities involved and, hence, higher operating temperatures. Although these materials have slightly higher conductivities, the higher operating currents negate any performance advantages these materials might offer to the MIRA-S thruster. The nozzle divergence angle (22.5 deg) and the anode-to-cathode radius ratios are the same for all three thrusters, whereas the area ratios are similar. Key dimensions for the three scaled thrusters are given in Table 1.

Test Facilities

All tests are conducted in a 0.5-m^3, polyvinyl chloride (PVC) vacuum tank with a nominal back pressure of 10^{-2} Pa. All of the instrumentation is housed in a full Faraday cage and data acquisition is computer controlled.

A thrust balance, shown in Fig. 1, and described in detail elsewhere,[11] is used to measure the thruster impulse bit and evaluate engine performance. Briefly, a thruster shot causes the thrust balance, suspended pendulum to oscillate. Simple pendulum theory provides the impulse bit

$$I_b = M_e \omega A$$

where M_e is the equivalent pendulum mass, ω is its natural frequency, and A is the maximum oscillation amplitude calculated by a computerized extrapolation of the damped pendulum oscillation.[11] The instantaneous position of the pendulum was measured using a magnetoinductive sensor of proximity, with a resolution of 0.001 mm.

Finally, the jet velocity measurement device is based on two double Langmuir probes located downstream of the thruster, aligned on the jet axis. Cross correlation of their signals provides an averaged time of flight of ions.[12] The measured ion velocity is actually an averaged value over all charged species in the plume and allows examination of how much jet exhaust energy resides in the charged species compared to the overall jet exhaust energy.

Test Procedures and Measurements

Experimental measurements include the instantaneous electrical characteristics [anode-to-cathode potential difference $V(t)$ and discharge current intensity $i(t)$], impulse bit I_b, jet velocity w, and ablated propellant mass per shot for each scaled thruster.

Values averaged over 12 measurements are used as the standard value for each electrical parameter and impulse bit, whereas a value averaged over 30 measurements is used for jet velocity.

Errors are calculated using error-propagation theory based on the standard deviation of the individual measurements because each data point represents many thruster shots.

The PFN provides input energies E_0 from 1333 to 3000 J in increments of 333 J. The PFN output energy was defined by setting the PFN potential V_0 according to

$$E_0 = \tfrac{1}{2} C V_0^2$$

The electrode potential is measured directly using an oscilloscope, whereas the current is measured using a Rogowsky probe. The thruster energy per shot

$$E_T = \int_0^\infty i(t) V(t) \, \mathrm{d}t$$

is computed using the measured electrical parameters.

The ablated propellant mass is obtained by weighing the propellant bars before and after each series of shots using an electronic balance with an accuracy of ± 1 mg. The error in this measurement has been estimated to be a maximum of ± 5 mg because of propellant handling and trigger insulator material ablation. The number of shots in each series is chosen so that the ablated mass exceeded 70–80 mg. Between 50 and 120 shots are required to achieve this result.

The PFN discharge characteristics (voltage and current profiles) depend on the PFN–thruster coupling and, specifically, the impedance matching between the thruster and the PFN. The time history of the nonsteady discharge current shows slightly different shapes depending on the thrusters and their regimes; it is, however, repeatable for each PFN–thruster combination and is characterized by a long tail where the current asymptotically approaches zero (Fig. 3).

To compare shots with different current-time histories, the current parameter Ψ is used, where

$$\Psi = \int_0^\infty i^2(t) \, \mathrm{d}t$$

This parameter effectively normalizes thruster behavior to allow direct comparisons of different thrusters and different PFN–thruster couplings.

The impulse bit I_b is related to Ψ through (often called the Maecker law)[13] (see also Ref. 14),

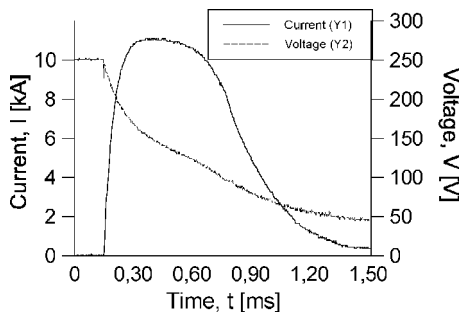$$(I_b)_{\text{th}} = (\mu/4\pi)\left[\ell n(r_a/r_c) + \tfrac{3}{4}\right]\Psi$$

where we can define

$$b = (\mu/4\pi)\left[\ell n(r_a/r_c) + \tfrac{3}{4}\right]$$

Here, b is the electromagnetic thrust coefficient and r_a and r_c are the average geometric radius of the anode and cathode radii, respectively. This equation permits an indirect determination of the impulse bit $(I_b)_{\text{th}}$ that is compared with directly measured I_b values.

Experimental Results

General Remarks

The first observation that can be made is that the discharges deposited a thin film of carbon and fluorine residues on the anode surface as result of the Teflon propellant ablation process. This relatively uniform coating led to an improvement in engine operability and repeatability.

Similarly, trigger electrode operation was improved by this same mechanism, as has been seen in previous testing.[2] The coating regulated the intensity of the discharge and was burned away when it became too thick.

However, when the trigger electrode insulator was consumed to the point that its terminus was inside the trigger electrode cavity in the center of the MPD cathode, the trigger function became erratic. At this point, the trigger discharge often failed to propagate outside the MPD cathode cavity, preventing the primary MPD shot from occurring.

Another mechanism that created MPD operational difficulties was the deposition of a carbonaceous residue across the Teflon insulator between the trigger electrode and MPD cathode. This created a short circuit condition that eliminated or severely limited the intensity of the trigger discharge. This phenomenon was particularly important in the operation of the MIRA-L, where the trigger electrode-to-MPD cathode distance was the greatest.

The baseline thruster, MIRA, was found to exhibit a behavior that was manifested in a statistical distribution of Ψ as a function of the number of thruster shots. This behavior appeared as two different operating modes in the wide, twin-peaked distribution of Ψ at a constant initial energy E_0, as shown in Fig. 4. A total of 400 thruster shots were used to generate Fig. 4. This twin-peaked behavior occurred for every thruster energy tested. These modes are denoted high and low with respect to the value of Ψ. Furthermore, as the initial energy E_0 increased, the high-mode behavior became increasingly dominant.

The internal anode faces of the two smaller thrusters showed very uniform azimuthal surfaces and the radial propellant bars showed equal and axisymmetric consumption after hundreds of shots. This uniformity implies a symmetrical azimuthal discharge current on average. These symmetries were not evident in the larger MIRA-L thruster.

Thruster Energy E_T

The thruster energy (propulsive energy) E_T as a function of the initial PFN set energy E_0 is linear, as shown in Fig. 5.
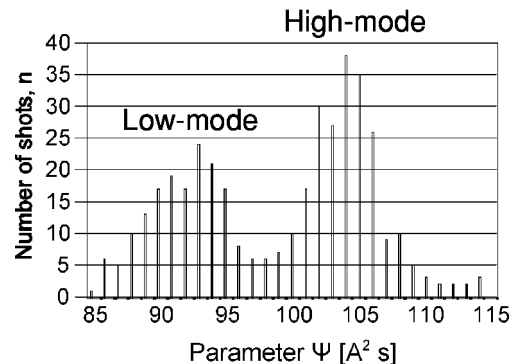
Fig. 3 Typical nonsteady, ablative MPD discharge current-voltage characteristic.

Fig. 4 Randomly generated twin-peaked behaviour of Ψ over 400 shots at a PFN initial energy of 2333 J for the MIRA thruster.
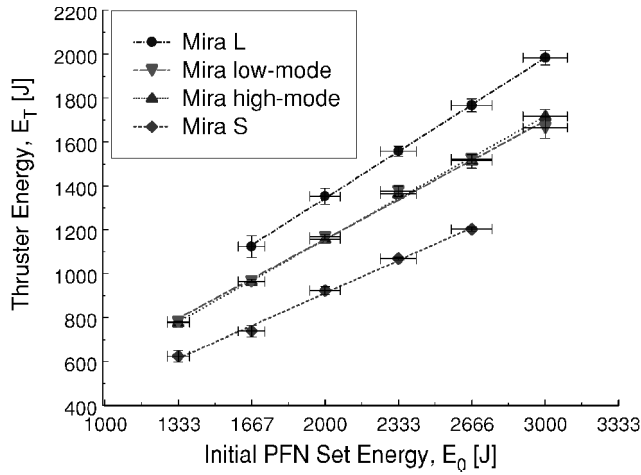
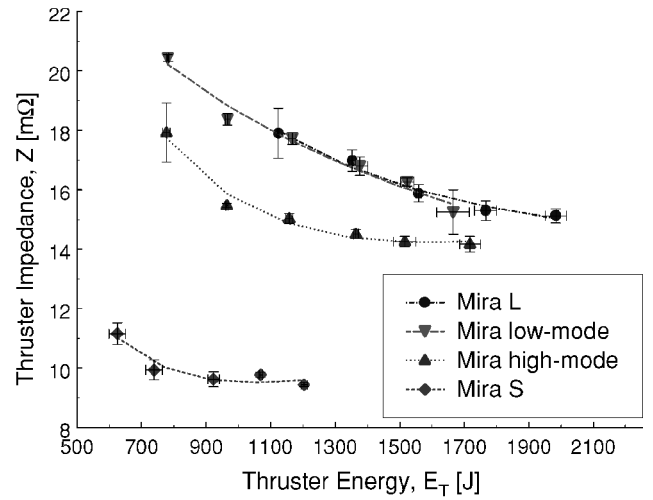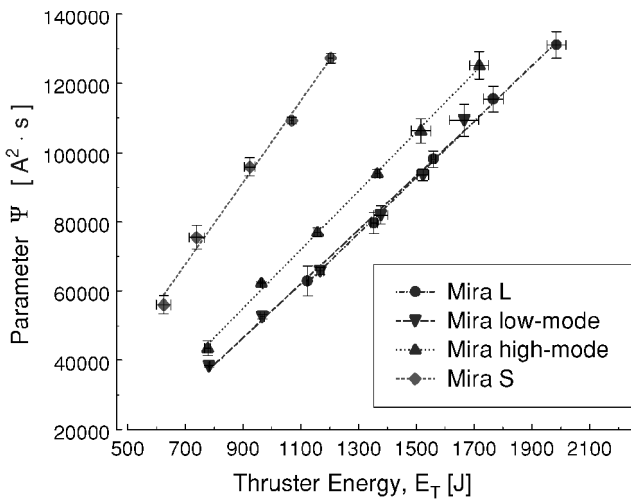Fig. 5   Linear relationship between thruster energy and input energy.

Fig. 6   Linear relationship between Ψ and E_T. Notice the twin operational modes of the MIRA thruster.

In spite of this linear relationship, different thrusters have different electrical transmission efficiencies,

$$\eta_{tr} = E_T / E_0$$

because they have different impedances. To compare thruster operation independently from the other components of the test system, the thruster energy E_T is taken as independent variable.

Parameter Ψ

For the thrusters tested here, Ψ increases linearly with E_T as shown in Fig. 6. Here, it can be seen that, for a given E_T, Ψ is highest for the MIRA-S, and lowest for the MIRA-L. The MIRA thruster high-mode falls between the small- and large-thruster characteristics, whereas the MIRA low-mode characteristic is effectively coincident with the MIRA-L characteristic.

Thruster Impedance

The thruster time-averaged impedance can be evaluated through the relationship

$$Z = E_T / \Psi$$

As shown in previous works[1,2,15] with different thrusters, the magnitude of the impedance has a tendency to decrease asymptotically to a limit value as shown in Fig. 7. Here, we see that although the thruster impedance-energy characteristic has the same basic shape in all cases, the MIRA high-mode and the MIRA-S characteristics fall below those of the effectively coincident MIRA-L and MIRA
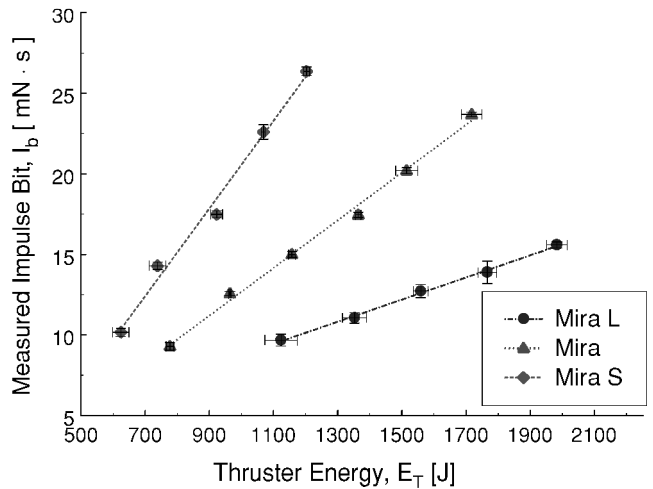

Fig. 7   Relationship between thruster impedance and thruster energy.

Fig. 8   Linear relationship between measured impulse bit and thruster energy.

low-mode characteristics. This is consistent with the Ψ-energy characteristics given in Fig. 6.

Impulse Bit

The measured impulse bit increases linearly with respect to the thruster energy E_T for all three thrusters (Fig. 8). Furthermore, as the thruster gets smaller, the impulse bit I_b gets larger at a fixed E_T as expected. (The increased current increases I_b.)

Propellant Consumption and Specific Energy

Propellant consumption m increased as thruster scale size decreased at constant thruster energy E_T (Fig. 9). This happens because the current intensity increases at fixed input energy as the thruster size decreases, which increases the ablative effects on the propellant bars.

The specific energy per propellant mass unit $E_{Tsp} = E_T/m$ varies strongly from thruster to thruster. Its value remains practically constant with increasing E_T, for the MIRA-S (between 650 and 625 J/mg) and for the MIRA-L (between 2020 and 2065 J/mg), whereas it decreases substantially from 1640 to 1310 J/mg for MIRA.

Jet Exhaust Velocity

The MIRA-L exhibited the highest measured velocities at high input energies, whereas the MIRA thruster showed the highest velocities everywhere else, as shown in Fig. 10.
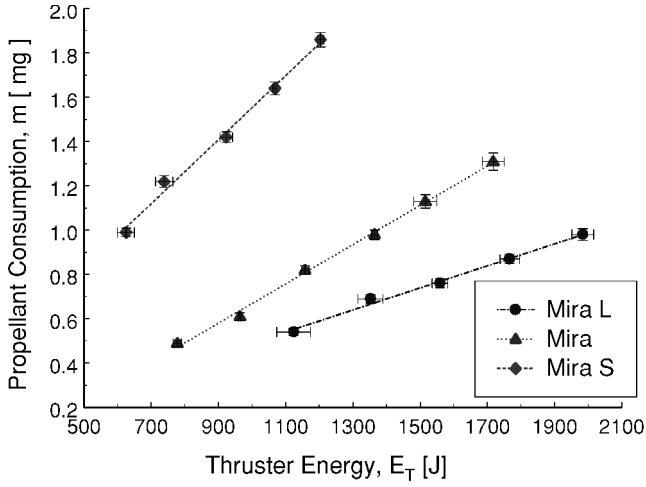
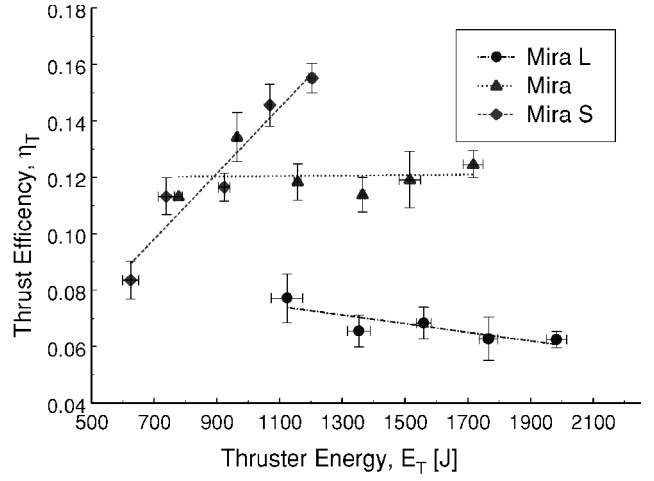Fig. 9   Propellant consumption increases as thruster scale decreases.

Fig. 11   Relationship between thrust efficiency and thruster energy.
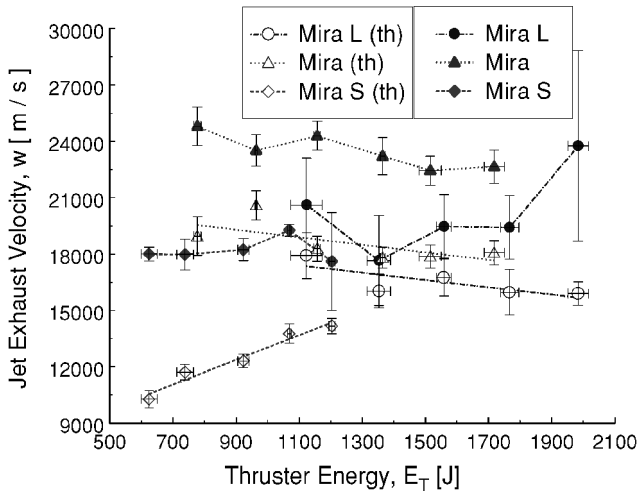

Fig. 10   Jet velocity is higher for larger scale size.

Fig. 12   Experimental data varies from the ideal in the relationship between I_b and Ψ, particularly in the MIRA-L.

An effective jet velocity, proportional to the specific impulse, has been calculated using

$$w_{\text{eff}} = I_b/m = g_0 I_{\text{sp}}$$

which corresponds to the theoretical values shown in Fig. 10.

Thrust Efficiency

The thrust efficiency

$$\eta_T = I_b^2 \big/ 2m E_T$$

is shown in Fig. 11 for the three thrusters as a function of the thruster energy. The efficiency decreases slightly with increasing energy in the MIRA-L thruster, remains relatively constant for the MIRA thruster, and increases strongly for the MIRA-S thruster. The MIRA-S thruster also exhibited the best performance at the higher thruster energies.

Remarks

Operating Modes of the MIRA Thruster

Several observations can be made regarding the two operating modes of the MIRA thruster. First, the propulsive energy E_T of the MIRA thruster is the same in both the high and low modes at fixed initial energy E_0 (Fig. 5). Therefore, the mode of thruster function is not dependent on the coupling of the thruster and PFN, but is a characteristic of the thruster.

Next, at an equal current parameter, the measured impulse bit assumes a lower value in the high-mode than in the low-mode (Fig. 12).
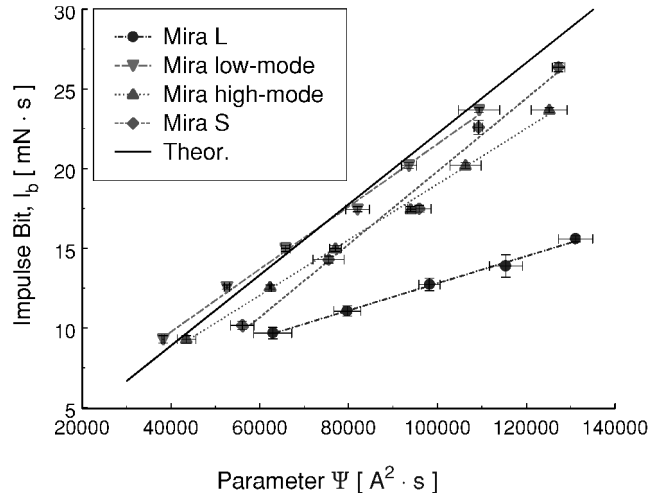
On the basis of the Maecker law,[13] a smaller thrust implies a smaller electromagnetic thrust coefficient. In Fig. 13, the effective thrust coefficient $b_{\text{eff}} = (I_b)_{\text{measured}}/(\Psi)_{\text{measured}}$, obtained by the use of the experimental data for each thruster operating point and mode, is shown as a function of Ψ: As for the expression of the thrust coefficient, a smaller b_{eff} implies that the arc is occurring in an area of smaller anode radius and vice versa.

Hence, in the high-mode, the anode current attachment region is upstream, deeper within the anode nozzle, modifying the morphology of the MPD discharge (Fig. 14).

This conclusion is confirmed by the value assumed by the ratio

$$\epsilon_T = \frac{(E_{T\text{sp}})_{E_T\text{max}}}{(E_{T\text{sp}})_{E_T\text{min}}} = \frac{(E_T/m)_{E_T\text{max}}}{(E_T/m)_{E_T\text{min}}}$$

which, for the MIRA thruster, is $\epsilon_{T\text{MIRA}} \approx 0.82$ (J/mg). In fact, this ratio can be used as an indicator of an axial shift of the discharge at increasing thrust energy E_T, where $\epsilon_T < 1$ represents a shift upstream and $\epsilon_T > 1$ a shift downstream.

An upstream movement of the arc corresponds to a reduction in the effective arc length and in the effective anode area. At fixed thruster energy, this results in a drop in the arc resistance and an increase in the current intensity. The increase in the current intensity and reduction in the effective anode area result in an increase of the current density. Moreover, an upstream movement of the arc implies an increasingly larger area of the propellant surface is exposed to a high-density discharge (Fig. 14) due to the position of the Teflon bars. All of this should result, at constant thruster energy, in an
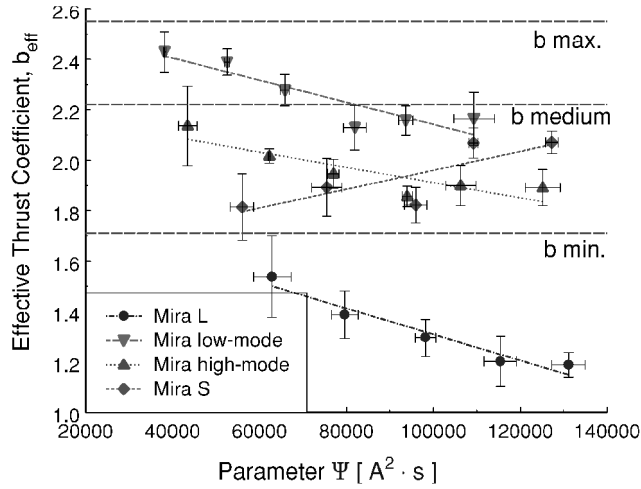
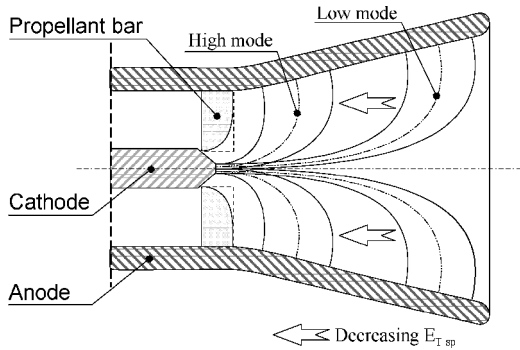Fig. 13 The MIRA-L effective thrust coefficient shows values which are not consistent with the Maecker law.
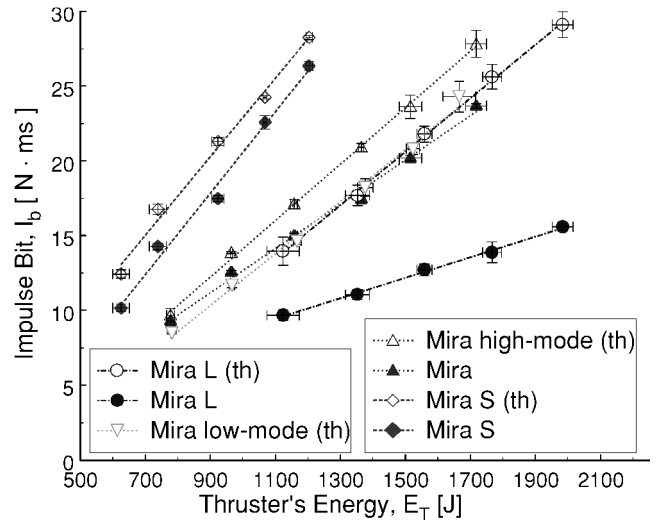

Fig. 15 The theoretical MIRA low-mode and MIRA experimental data for impulse bit characteristics are very similar. In the MIRA high-mode and MIRA-S the theoretical impulse bit characteristics differ significantly from experimental values; in MIRA-L the gap is extremely large.

Fig. 14 Simplified schematic of MPD thruster operation.

increase in propellant consumption, that is, a reduction of the specific energy $E_{T\,\mathrm{sp}}$.

Hence, because at $E_{T\,\mathrm{max}}$ the MIRA thruster functions practically only in high-mode and vice versa at $E_{T\,\mathrm{min}}$, a ratio $\epsilon_T < 1$ indicates that the arc is occurring in an area of smaller anode radius in the high-mode.

That the b_{eff} diminishes at increasing current parameter is in accordance with previous findings of a work on a segmented-anode MPD thruster.[15] This work showed that anode current attachment does not exhibit a uniform axial distribution. In fact, it was shown that (using a four-segment anode with similar dimensions to MIRA), as E_T increases, the peak values of the Ψ distribution move upstream within the thruster to the point where the anode has the smallest radius, thus reducing the b_{eff}.

Consistent with the preceding observations, when the I_b vs E_T characteristics are compared to Maecker's law[13] predictions (Fig. 15), the theoretical predictions closely match only MIRA low-mode behavior. The explanation lies within the contributions to the electromagnetic thrust coefficient from the axial and radial components of the electromagnetic force that combine to produce thrust. As shown in Fig. 14, the current attachment region to the anode is always downstream of the cathode tip. The current density has directed components that produce the radial component of force through interaction with the self-generated magnetic field. As the arc moves upstream, that is, for smaller b_{eff}, the axial component is reduced because the cathode-to-anode radius ratio drops. Furthermore, if the current distribution becomes purely radial, the radial thrust component drops (theoretically) to zero.

Therefore, because the MIRA low-mode operation occurs when the current attachment region is downstream in the nozzle, the radial component is maximized, while at the same time allowing current attachment at an anode radius that closely matches the average anode radius r_a used in the theoretical calculations.

Scaled Thrusters

The MIRA-L thruster behaves like the baseline MIRA thruster in low-mode (Fig. 6). It appears to operate in a regime characterized by lower current densities due to its larger interelectrode distances and larger effective anode area. On the contrary, the MIRA-S operates in a regime with higher current densities. The MIRA thruster high-mode behaves more like the MIRA-S thruster. As shown in Fig. 9, propellant consumption increases faster than the rate of decrease in scale size. This is particularly true for the case of the MIRA-S. MIRA thruster propellant ablation occurs partially in a low-mode and partially in a high-mode regime.

Moreover, because in the scaled thrusters the specific energy (E_T/m) is the same in all of the different regimes, the operating mode remains stable in each thruster as E_T varies. Nevertheless, the specific energy has strongly different values in these two thrusters.

Maecker's law[13] says that the relationship between impulse bit I_b and Ψ should be linear, and the characteristics for scaled thrusters (with equal anode to cathode radius ratio), should collapse into a single straight line. As can be seen in Fig. 12, the basically linear behavior is shown experimentally, but dispersion from a single curve can be seen as expected based on the earlier considerations. The MIRA-S characteristic has the steepest slope and most closely matches the slope of the theoretical curve calculated with $r_a = r_{a\,\mathrm{medium}}$. The MIRA-L characteristic has the shallowest slope and shows a strong divergence from the theoretical curve.

The different operating regimes of the thrusters are also shown through the b_{eff} characteristics as a function of Ψ (Fig. 13). Figure 13 also shows three theoretical values of the Maecker[13] coefficient calculated assuming anode radii of minimum (b_{min}), medium (b_{med}), and maximum (b_{max}) values, respectively. The MIRA-S effective thrust coefficient shows a positive slope, in contrast to the others, which have negative slopes. The b_{eff} values of the MIRA low-mode fall around the b_{med} theoretical value, whereas the b_{eff} values of the MIRA high-mode and MIRA-S fall between b_{med} and b_{min}. On the contrary, the b_{eff} values for the MIRA-L thruster are much smaller than the minimum theoretical value. Therefore, Maecker's law[13] can not be used to provide the impulse bit for the MIRA-L thruster.

In the MIRA-L jet, the double Langmuir probes provided weak and irregular signals (Fig. 10). Because these signals are a function of the plasma density, it can be inferred that the plasma jet was not homogeneous and that the azimuthal current symmetry was weak. The MIRA-L velocity values vary over a much wider range than the ion velocities measured in the smaller-sized thrusters. Therefore, the fundamental symmetries that support the Maecker law[13] are not present in the MIRA-L thruster, leading to a divergence from theoretical predictions (Fig. 12).

The thrust stand-derived specific impulse values are substantially smaller than specific impulse values based on measured velocities, though the effect is less pronounced for the MIRA-L thruster (Fig. 10). This indicates that the exhaust jet includes neutral species as part of the overall thruster I_b, which can not be measured using an ionic species-based time-of-flight technique with double Langmuir probes.

In addition, in the MIRA-S, the gap between the measured velocity and the specific impulse tends to decrease for increasing energy. This implies that the ratio of ionized to non-ionized species is decreasing.

In previous papers on segmented anode thrusters,[15,16] it was shown that the discharge displacement varies during a shot as the anode current attachment region moves upstream. In the present case, consistent with this behavior, the thruster impedance has, in the middle phase of the shots, a decreasing time history (Fig. 3).

Magnetic Reynolds Number

The regime of the stream in a thruster may be characterized by the ratio between the convection and the diffusion of the magnetic field, that is, by the magnetic Reynolds number

$$Re_m = \mu_0 \sigma w L$$

where L is a characteristic length of the thruster. This parameter increases as a function of the thruster specific energy and, hence, as the discharge concentrates downstream.[17,18]

When an averaged value is assumed, the magnetic Reynolds number in the MIRA low-mode is given by $(\overline{Re_m})_{\text{MIRA-LM}} = \mu_0 \bar{\sigma}_{\text{MIRA-LM}} \bar{w}_{\text{MIRA-LM}} L_{\text{MIRA-LM}}$. The ratio

$$\rho_R = \frac{Re_m}{(\overline{Re_m})_{\text{MIRA-LM}}}$$

where Re_m is given for a generic thruster or regime, can be used to compare the different thrusters and regimes. Because $\sigma = (1/Z)(l/S)$, where l and S are the length and the section area of the discharge, respectively, the magnetic Reynolds numbers ratio ρ_R for scaled thrusters can be written,

$$\rho_R = (\bar{Z}_{\text{MIRA-LM}}/Z)(w/\bar{w}_{\text{MIRA-LM}})$$
$$\times [(l/\bar{l}_{\text{MIRA-LM}})(\bar{S}_{\text{MIRA-LM}}/S)(L/\bar{L}_{\text{MIRA-LM}})] = \rho_{R0}A$$

where

$$A = (l/\bar{l}_{\text{MIRA-LM}})(\bar{S}_{\text{MIRA-LM}}/S)(L/\bar{L}_{\text{MIRA-LM}})$$

and

$$\rho_{R0} = (\bar{Z}_{\text{MIRA-LM}}/Z)(w/\bar{w}_{\text{MIRA-LM}})$$

is the value that ρ_R would have assumed if the discharge would have the same form in every thruster and functioning mode. When the values of the latter parameter for each thruster and mode are computed, the theoretical predictions (ρ_R increasing with E_{Tsp}) requires that

$$0.90(A)_{\text{MIRA-L}} > 1(A)_{\text{MIRA-LM}} > 1.15(A)_{\text{MIRA-HM}} > 1.62(A)_{\text{MIRA-S}}$$

This is true only if the discharge concentrates downstream, thus increasing the length l and, as a consequence, the parameter A. Irrespective of this, the magnetic Reynolds number has similar values in the different thrusters and modes.

Conclusions

An experimental investigation of engine scale effects on solid-propellant MPD thruster operation has been presented. Three thrusters were tested: the MIRA thruster, the MIRA-S thruster, and the MIRA-L thruster. The MIRA thruster was found to operate in one of two electrical modes, in a random fashion, at a fixed energy, namely, low and high. As the absolute energy level was increased, the frequency of high-mode operation was found to increase. No significant differences were noted in impulse bit or exhaust velocity characteristics, but the Maecker law[13] coefficient b was found to be approximately 15% higher in MIRA high-mode as a function of Ψ. The scaled thrusters (smaller and larger) operated in only one electrical mode.

These tests showed that the MIRA-S provided a higher impulse bit at a fixed energy, as expected. The MIRA-S and baseline MIRA thrusters exhibited generally flat exhaust velocity profiles. The MIRA thruster, in low-mode, exhibited the highest Maecker law[13] coefficient as a function of discharge energy. The MIRA and MIRA-L thruster Maecker law coefficients exhibited approximately equal negative slopes as a function of Ψ, whereas the MIRA-S thruster exhibited a positive slope. Finally, the efficiency of the MIRA-S thruster was found to increase strongly with thruster energy, whereas the efficiencies of the other two thrusters remained constant or decreased slightly. These data imply that the smaller thruster operates in a different regime than the larger thrusters. This operational regime difference is likely related to the smaller specific energy and to the higher current densities in the smaller thruster.

References

[1]Paccani, G., "Non-Steady Solid Propellant MPD Thruster Experimental Analysis Concepts," AIAA Paper 90-2674, July 1990.

[2]Paccani, G., Chiarotti, U., and Deininger, W. D., "Quasi-Steady Ablative Magnetoplasmadynamic Thruster Performance with Different Propellants," *Journal of Propulsion and Power*, Vol. 14, No. 2, 1998, pp. 254–260.

[3]Mead, F. B., and Jahn, R. G., "Scaling of MPD Thrusters," AIAA Paper 79-2075, Oct. 1979.

[4]Kaplan, D., and Jahn, R. G., "Performance Characteristics of Geometrically Scaled MPD Thrusters," Rept. 1942, Dept. of Mechanics and Aerospace Engineering, Princeton Univ., Princeton, NJ, Feb. 1982.

[5]Andrenucci, M., Paganucci, F., Grazzini, P., and Pupilli, F., "Scale and Geometric Effects on MPD Thrusters," AIAA Paper 92-3159, July 1992.

[6]Gilland, J. H., Kelly, A. J., and Jahn, R. G., "MPD Thruster Scaling," AIAA Paper 87-0997, May 1987.

[7]Orlandi, A., Baiocchi, G., Borriello, G., and Carabella, G., "Solid Propellant MPD Thruster Development," AIAA Paper 85-2066, Sept. 1985.

[8]Petrucci, L., "Propulsori MPD in Scala," LAUREA Thesis, Facoltà di Ingegneria, Univ. of Rome "La Sapienza," Rome, Feb. 1996 (in Italian).

[9]Paccani, G., "Studi sui Meccanismi Fisici di Base nei Propulsori MPD," Secondo Rapporto Intermedio, Italian Space Agency, Contratto di Ricerca ASI 92-RS-27, Rome, July 1994 (in Italian).

[10]Andrenucci, M., and Lensi, R., "Designing Solid Propellant MPD Thrusters," AIAA Papers 79-2059, Oct. 1979.

[11]Paccani, G., and Ravignani, R., "Sistemi di Misura della Spinta di Propulsori MPD," *Aerotecnica Missili e Spazio*, Vol. 72, No. 1, 1994, pp. 42–51 (in Italian).

[12]Paccani, G., and Di Zenzo, S., "Computerized Jet Velocity Measurements in MPD Thrusters," *Aerotecnica Missili e Spazio*, Vol. 74, Nos. 3–4, 1995, pp. 93–102.

[13]Maecker, H., "Plasmaströmungen in Licht-Bögen Infolge Eigenmagnetischer Kompression," *Zeitschrift für Physik*, Bd. 141, 1955, pp. 198–216 (in German).

[14]Jahn, R. G., "Physics of Electric Propulsion," McGraw–Hill, New York, 1968, Chap. 8.

[15]Paccani, G., "Experimental Analysis of a Coaxial Solid Propellant MPD Thruster with Segmented Anodes," AIAA Paper 93-159, Sept. 1993.

[16]Paccani, G., "Studi sui Meccanismi Fisici di Base nei Propulsori MPD," Primo Rapporto Intermedio, Italian Space Agency, Contratto di Ricerca ASI 92-RS-27, Rome, April 1993 (in Italian).

[17]Barnett, J., and Jahn, R. G., "MPD Thruster Operation with Stepped Current Input," JSASS/AIAA/DGLR 17th IEPC, IEPC Paper 84-57, Tokyo, Japan, May 1984.

[18]Yoshikawa, T., Kagaya, Y., Yokoy, Y., and Tahara, H., "Performance Characteristics of Quasi-Steady MPD Thrusters," JSASS/AIAA/DGLR 17th IEPC, IEPC Paper 84-58, Tokyo, Japan, May 1984.